ARTICLE OPEN

High-temperature phonon-mediated superconductivity in monolayer $Mg_2B_4C_2$

Sobhit Singh[1]✉, Aldo H. Romero[2]✉, José D. Mella[3,4], Vitalie Eremeev[5], Enrique Muñoz[6], Anastassia N. Alexandrova[7,8], Karin M. Rabe[1], David Vanderbilt[1] and Francisco Muñoz[4,9]✉

A two-dimensional material – $Mg_2B_4C_2$, belonging to the family of the conventional superconductor MgB_2, is theoretically predicted to exhibit superconductivity with critical temperature T_c estimated in the 47–48 K range (predicted using the McMillian-Allen-Dynes formula) without any tuning of external parameters such as doping, strain, or substrate-induced effects. The origin of such a high intrinsic T_c is ascribed to the presence of strong electron-phonon coupling and large density of states at the Fermi level. This system is obtained after replacing the chemically active boron-boron surface layers in a MgB_2 slab by chemically inactive boron-carbon layers. Hence, the surfaces of this material are inert. Our calculations confirm the stability of 2D $Mg_2B_4C_2$. We also find that the key features of this material remain essentially unchanged when its thickness is increased by modestly increasing the number of inner MgB_2 layers.

npj Quantum Materials (2022)7:37 ; https://doi.org/10.1038/s41535-022-00446-6

INTRODUCTION

The discovery of highly crystalline two-dimensional (2D) superconductors[1–5], such as $NbSe_2$ monolayer[6–9], has provided possibilities for van der Waals (vdW) heterostructures nanoengineering of insulator-superconductor interfaces[10] and 2D Josephson junctions, without the need of an insulating layer[11]. One main challenging issue in the realization of 2D superconductivity is that most of the well-known conventional bulk superconductors either do not superconduct or poorly superconduct when their dimensions are reduced[6–8,12–17]. Although numerous 2D phonon-mediated superconductors have recently been predicted from first-principles calculations, the highest predicted intrinsic T_c stayed around 20 K[17–24] (19 K for B_2C monolayer[21], 10.3 K for B_2O monolayer[17], and 19–25 K for borophenes[22], to name a few). Though in some cases T_c has been enhanced by means of the chemical doping, intercalation, strain, and/or substrate proximity effects[17,23,25–32], it is essential to discover intrinsic 2D superconductors that exhibit high-T_c without any doping or tuning of external parameters (here high-T_c does not refer to unconventional superconductivity as in case of cuprates or iron-based superconductors[33]).

Among all the Bardeen–Cooper–Schrieffer (BCS) type conventional superconductors, MgB_2 stands out with a record T_c of 39 K, the highest reported T_c at zero-pressure[34–36]. Such a high-T_c in MgB_2 stems from the strong electron-phonon (el-ph) coupling occurring primarily due to the in-plane stretching of B-B bonds (i.e., E_{2g} phonon modes), which strongly couple with the self-doped charge carriers from magnesium to boron atoms[26,35–38]. Remarkably, only two (E_{2g}) out of a total of nine phonon modes contribute strongly to the total el-ph coupling in MgB_2[35–44]. Once the fundamental mechanism of such a high-T_c in bulk MgB_2 was understood, which by the way was a subject of intense research for over a decade period[26,35–49], researchers started proposing ways to augment T_c through rational materials design approach[25,37,43,44,50–52]. Pickett and co-workers proposed that one can, in principle, achieve a much higher T_c (than 39 K) by designing a MgB_2-like stable material that has a similar Fermi surface as in MgB_2, and in which more than two phonon modes couple to the electronic states near the Fermi level, thereby, resulting in a sizable total el-ph coupling[25,43,44]. This idea has been employed for the rational design of bulk superconductors with a good success rate[53–64]. The high-pressure superconductivity observed at 250 K in lanthanum hydride is one such example[65–68].

Despite the large success with the bulk conventional superconductors, two-dimensional intrinsic superconductors having a high-T_c remained elusive. Notably, various attempts have been made to realize superconductivity in the 2D analogues of bulk MgB_2[13,32,51,69–74]. On the one hand, Xu and Beckman proposed a quasi-2D MgB_2 nanosheet with inert surfaces, which turns out to be a semiconductor with a bandgap of 0.51 eV resulting from the quantum confinement effects[13]. On the other hand, Bekaert et al. reported that a considerably high-T_c of 20 K can be realized in monolayer MgB_2 without surface passivation, i.e., if only such a material with a highly chemically reactive surface could be made[73,74]. In a recent study, Bekaert et al. theoretically demonstrated that a MgB_2 monolayer can be stabilized by adding hydrogen adatoms. Interestingly, they find that the hydrogenation process leads to a high-T_c of 67 K, which can be further boosted to over 100 K by means of a biaxial strain on the hydrogenated MgB_2 monolayer[32]. While an experimental validation of the predicted T_c in monolayer MgB_2 is still missing, the aforementioned theoretical works markedly enhance our understanding of superconductivity in 2D materials.

In this work, we present a MgB_2-like 2D material – $Mg_2B_4C_2$, having charge neutral inert surfaces, which is predicted to

[1]Department of Physics and Astronomy, Rutgers University, Piscataway, New Jersey 08854, USA. [2]Department of Physics and Astronomy, West Virginia University, Morgantown, West Virginia 26506, USA. [3]Departamento de Física, Facultad de Ciencias Físicas y Matemáticas, Universidad de Chile, Santiago 8370449, Chile. [4]Departamento de Física, Facultad de Ciencias, Universidad de Chile, Santiago 7800024, Chile. [5]Instituto de Ciencias Básicas, Facultad de Ingeniería y Ciencias, Universidad Diego Portales, Santiago 8370191, Chile. [6]Institute of Physics, Pontificia Universidad Católica de Chile, Santiago 7820436, Chile. [7]Department of Chemistry and Biochemistry, University of California, Los Angeles, CA 90095, USA. [8]California NanoSystems Institute, Los Angeles, CA 90095, USA. [9]Center for the Development of Nanoscience and Nanotechnology (CEDENNA), Santiago 9170022, Chile. ✉email: sobhit.singh@rutgers.edu; Aldo.Romero@mail.wvu.edu; fvmunoz@u.uchile.cl

superconduct at a strikingly high-T_c in the 47–48 K range (predicted using the McMillian-Allen-Dynes theory[75–77]), which is among the highest T_c yet reported for an intrinsic 2D material without any doping, strain or substrate-induced effects. The main advantageous feature in 2D $Mg_2B_4C_2$ is the fact that, unlike in bulk MgB_2, more than two phonon modes strongly couple to the electronic states near the Fermi level, thus, resulting in a substantially larger el-ph coupling ($\lambda = 1.40$) in monolayer $Mg_2B_4C_2$ compared with the bulk MgB_2 ($\lambda_{bulk} = 0.73$[38], and 0.61[36]). We note that the estimated λ in monolayer $Mg_2B_4C_2$ is comparable to the predicted $\lambda = 1.46$) in hydrogenated MgB_2 monolayer[32]. Moreover, our calculations reveal nontrivial topological electronic features in $Mg_2B_4C_2$ exhibiting Dirac cones and practically gapless Dirac nodal lines at the Fermi level near the corner points of the hexagonal Brillouin zone (BZ), which enhance the density of states (DOS) at the Fermi level by almost 30% compared to that of bulk MgB_2, hence, positively contributing towards a higher T_c.

RESULTS AND DISCUSSION

Material design strategy

We start by describing our rationale for design of a stable MgB_2-like 2D superconductor having inert surfaces. Generally, layered vdW materials can be exfoliated to produce their 2D analogues[78]. Although bulk MgB_2 has a layered structure, it is not a vdW material. Bulk MgB_2 crystallizes in space group P_6/mmm (#191) containing alternating layers of Mg and B atoms stacked along the $\vec{c}$ lattice direction, as shown in Fig. 1(a)[42]. The bonding between the Mg and B atoms is purely ionic, which means that Mg atoms donate two electrons to B atoms, thereby making each Mg 2^+ and each B 1^-. Since a B^- is isoelectronic to a charge-neutral carbon atom, a B-B sheet is structurally analogous to a single layer graphene, but it has a different ordering of bands than those of graphene. A simple exfoliation of MgB_2 into a 2D slab with B (or Mg) termination would yield a highly reactive electron-rich (or hole-rich) surface layer that is chemically unstable.

We propose that one can passivate the charged surface layers in the MgB_2 slab by systematically substituting one boron by one carbon atom at the top and bottom surfaces of the slab. Figure 1 (b) shows the top and side views of a $Mg_2B_4C_2$ monolayer designed using the aforementioned strategy. Strikingly, we find that modestly repeating the intermediate Mg-B layers, *i.e.*, the layers sandwiched between the top and bottom surfaces (highlighted using dashed rectangle in Fig. 1(b)), thereby making thicker slabs of $(MgB_2)_nC_2$ while remaining in the quasi-2D limit, n being the total number of Mg layers, retains the key features of

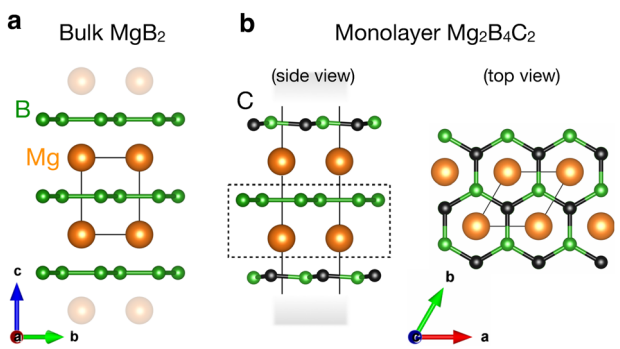

Fig. 1 Crystal structure. a Bulk MgB_2, and (**b**) side (as viewed from $\vec{a}$) and top views of monolayer $Mg_2B_4C_2$ (Mg: orange, B: green, C: black). Solid black lines mark the unit cell boundaries, and shaded grey areas represent vacuum in the left panel of (**b**). The region marked by dashed black lines in (**b**) can be arbitrarily repeated (see text).

the $Mg_2B_4C_2$ monolayer. The electronic bandstructures calculated up to $n = 5$ are shown in the Supplementary Fig. 1. This feature could be particularly useful in the experimental realization of 2D superconductivity in $Mg_2B_4C_2$. We note that MgB_2 monolayer can also be passivated by an appropriate hydrogenation process[32].

$Mg_2B_4C_2$ monolayer, shown in Fig. 1(b), belongs to the layer group $p\bar{3}m1$ (#72) having DFT (PBE) optimized lattice parameters $a = b = 2.87$ Å. The absolute thickness between the top and bottom atomic layers is 7.14 Å, whereas, the interlayer spacing between the adjacent Mg and B-B, and Mg and B-C (C-B) layers is ~1.8 Å, and ~1.7 Å, respectively. We note that the inversion symmetry is preserved due to the inverted ordering of the top and bottom layers in the structure shown in Fig. 1(b). However, one could break the inversion symmetry by replicating the top and bottom layers, i.e., by making the top and bottom layers alike, either both as B-C or both as C-B. Our calculations suggest that the structure with inversion symmetry is energetically more favorable (5 meV/f.u.) than the structure with broken inversion symmetry; although both structures are dynamically, elastically, and mechanically stable since they exhibit all positive phonon frequencies, positive elastic constants, and satisfy the Born-Huang mechanical stability criteria (see Supplementary Table 2 and Supplementary Fig. 6). The only qualitative difference in the electronic properties of the structure with broken inversion symmetry is a small lifting of some band degeneracies at the K high symmetry point (see Supplementary Fig. 3). This effect is analogous to the application of a perpendicular electric field to a bilayer graphene[79].

In this article, hereafter, we focus only on ground state structure of a monolayer $Mg_2B_4C_2$ with preserved inversion symmetry. We note, all other possible atomic configurations of this composition are higher in energy. Furthermore, our exfoliation energy calculations (see Supplementary Table 3) suggest that the reported monolayer $Mg_2B_4C_2$ belongs to the "easily exfoliable" category, as classified by Mounet et al.[80].

Topological electronic properties of $Mg_2B_4C_2$ monolayer

After describing the crystal structure and its stability, we now focus on the topological electronic properties of $Mg_2B_4C_2$ monolayer. We begin by summarizing the key features of the electronic structure of bulk MgB_2[42] from which $Mg_2B_4C_2$ monolayer is derived. As shown in Fig. 2(a), the Fermi surface of MgB_2 is composed of boron p orbitals, where $p_{x,y}$ orbitals hybridize with s orbitals to form strong covalent in-plane σ bonds at the zone center, while the unhybridized p_z orbitals form relatively weak out-of-plane π bonds at zone boundaries (Mg acts as electron donor). Due to such a distinct Fermi-surface geometry, two superconducting gaps exists in bulk MgB_2: (i) the stronger σ gap of ~7 meV, and (ii) the weaker π gap of ~2–3 meV[35,36,39,46,81–85]. Different symmetries of the σ and π bonds largely suppress the impurity scattering in MgB_2[39,41,42,85].

Since the basic structure and charge neutrality of MgB_2 is preserved in monolayer $Mg_2B_4C_2$, the electronic band structure of monolayer $Mg_2B_4C_2$ qualitatively resembles with that of the bulk MgB_2, as shown in Fig. 2(a, b), but with some additional features. For instance, there is a set of degenerate σ bands (σ_{outer}) present at Γ below the Fermi level arising from the $p_{x,y}$ orbitals of the outer boron-carbon layers. The other set of degenerate σ bands (σ_{inner}) at Γ that cross the Fermi level (also present in MgB_2) are formed by the $p_{x,y}$ orbitals of the inner boron-boron layer. These two sets of σ bands are almost parallel and split by ~1.6 eV at Γ. Since the σ_{outer} bands are completely occupied, they should, in principle, have no contribution in superconductivity, unless there is a large external field applied in a FET-like geometry[86].

In addition to the set of σ bands at Γ, we notice the presence of Dirac-like band crossings at the K point, as well as along the high-symmetry directions near the K point of monolayer $Mg_2B_4C_2$.

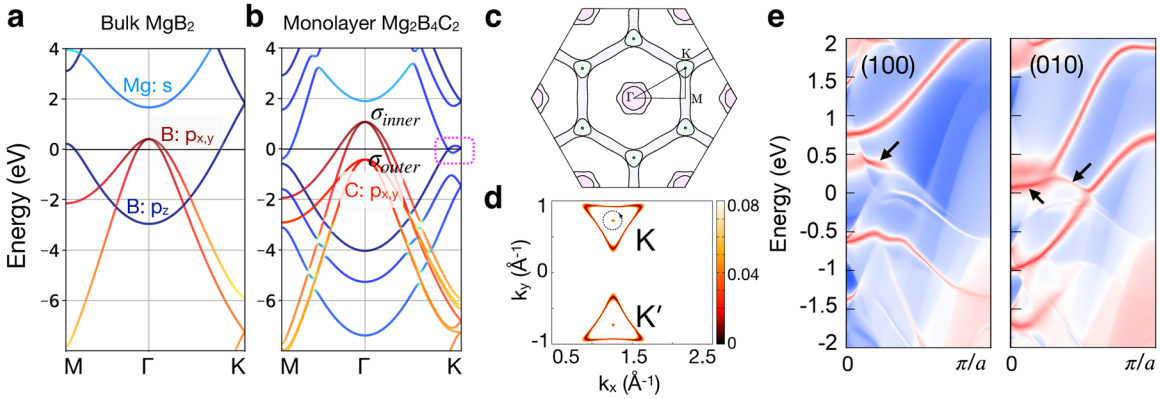

Fig. 2 Electronic structure. Atomic orbitals projected electronic band structure of (**a**) bulk MgB_2, and (**b**) monolayer $Mg_2B_4C_2$ calculated without spin-orbit coupling (SOC) along the high symmetry direction of BZ. Cyan, red, and blue colors represent the contribution from the s, $p_{x,y}$, and p_z orbitals, respectively. See Supplementary Fig. 4 for more details. **c** Calculated Fermi surface of monolayer $Mg_2B_4C_2$. Light pink/green, and grey colors depict hole/electron, and intertwined electron-hole pockets, respectively. **d** Energy bandgap (E_{gap}) plotted in color scale (eV units) in the vicinity of a K high-symmetry point. The dashed circle marks the *k*-loop along which Berry phase was computed. **e** The local electronic density of states of the (100) and (010) edge states spectrum. Red/White color denotes the states near the edge/interior of the 2D system. Topological nontrivial edge states are marked using arrows.

Table 1. Parity eigenvalues of all occupied bands and their products at four TRIM points.

TRIM	Parity eigenvalues	δ
Γ (0, 0, 0)	+ − + − + − + + − − + +	−1
M_1 (0.5, 0.0, 0.0)	− + − + − + + − + − − −	−1
M_2 (0.0, 0.5, 0.0)	− + − + − + + − + − − −	−1
M_3 (0.5, 0.5, 0.0)	− + − + − + + − + − − +	+1

Regardless of their topological nature, these band crossings at the Fermi level, highlighted using a dashed magenta box in Fig. 2(b), yield a large DOS at the Fermi level (almost 30% larger than in bulk MgB_2), which contributes substantially to the total el-ph coupling in the studied monolayer. We note that the Dirac-like crossing at K is also present in bulk MgB_2, but it is situated well-above the Fermi level[87]. The Dirac-like band crossings in $Mg_2B_4C_2$ monolayer are formed by highly dispersing p_z orbitals of carbon and boron atoms (see Supplementary Fig. 4). Thus, the Fermi surface of $Mg_2B_4C_2$ monolayer, shown in Fig. 2(c), embodies three main features: (i) two-hole pockets at Γ (one circular and another that takes the shape of the BZ) composed of σ bonded boron $p_{x,y}$ orbitals, (ii) an electron pocket at M formed by boron p_z orbitals, and (iii) intertwined electron and hole pockets at the K point and along K–M high-symmetry line, formed by π bonded carbon and boron p_z orbitals. We note that all these pockets show very strong coupling to the phonon modes, and, as a result, they play the key role in governing superconductivity in $Mg_2B_4C_2$ monolayer, as we discuss later. Furthermore, the sharp and well-defined (almost flat) boundaries of the charge-carrier pockets at the Fermi surface set up the stage for the possible realization of Kohn-like divergencies[88], and charge-density-wave ordering[89,90] in this 2D system, which is beyond the scope of present work and calls for a more comprehensive attention in the future.

By plotting the energy bandgap (E_{gap}) distribution in the vicinity of the K points, we discover presence of a triangular nodal line in the vicinity of each K point, as shown in Fig. 2(d). However, this is not a truly gapless nodal line since a small E_{gap} (~5 meV) exists due to the subtle breaking of M_z mirror symmetry. It is worth noting that the Dirac point at K is protected by the C_{3v} rotation, inversion, and time-reversal symmetries; a small gap opens at Dirac points when the inversion symmetry is broken by making the top and bottom B-C layers identical[91]. Although there are theoretical proposals suggesting the possibility of topological superconductivity in Dirac semimetals[92], we think that the so-far studied models are quite simple, and this topic requires a more thorough examination before any exotic effects can be confidently claimed here.

In order to prove the nontrivial topological nature of Dirac points, we compute the Berry phase along a *k*-loop enclosing the gapless point at K, as marked using dashed lines in Fig. 2(d). Our calculations yield a nontrivial Berry phase of π for Dirac points at K. We note, this exercise could not be performed for the Dirac nodal line near K because enclosing the nodal line residing in the k_x-k_y plane would require a *k*-loop encircling along k_z and k_z is not defined for a 2D system. Nevertheless, the presence of time-reversal and spatial-inversion symmetries of $Mg_2B_4C_2$ monolayer enables us to determine the Z_2 topological invariants using the Fu-Kane criterion[93]. The inversion parity eigenvalues of the electronic wavefunction of all 12 occupied bands at four time-reversal invariant momenta (TRIM) points are given in Table 1. The product of all parity eigenvalues (δ) at each TRIM is also listed in Table 1. We find that the Z_2 topological index is nontrivial due to $\delta = -1$ at three TRIM points. Here, we note that bulk MgB_2 has a weak Z_2 topological index (0; 001) due to the band-inversions occurring at the Γ and *A* (0, 0, 0.5) high-symmetry points of 3D hexagonal BZ[87]. Robust topological surface states have recently been experimentally observed in bulk MgB_2[94].

Since the nontrivial topology in 2D systems is often manifested in the gapless 1D edge states, we further confirm the nontrivial topological features of monolayer $Mg_2B_4C_2$ by computing the local density of states at (100) and (010) edges of 60 unit cell thick nano-ribbons. Topologically nontrivial 1D edge states connecting band-crossing points were obtained at both (100) and (010) edges, as shown in Fig. 2(e), thus, proving the nontrivial topology of the $Mg_2B_4C_2$ monolayer.

Electron-phonon coupling and superconductivity in $Mg_2B_4C_2$

We find that the roots of superconductivity in $Mg_2B_4C_2$ monolayer are the same as in bulk MgB_2[35–44]. However, the main advantageous factor in $Mg_2B_4C_2$ is that, in addition to the doubly degenerate E_{2g} modes that govern superconductivity in MgB_2, numerous other phonon modes strongly couple to the electronic states near the Fermi level yielding a much larger overall el-ph coupling, and thus, resulting in a considerably higher T_c.

The calculated phonon spectrum of $Mg_2B_4C_2$ monolayer, shown in Fig. 3(a), contains a total of 24 phonon modes (8 atoms/cell)

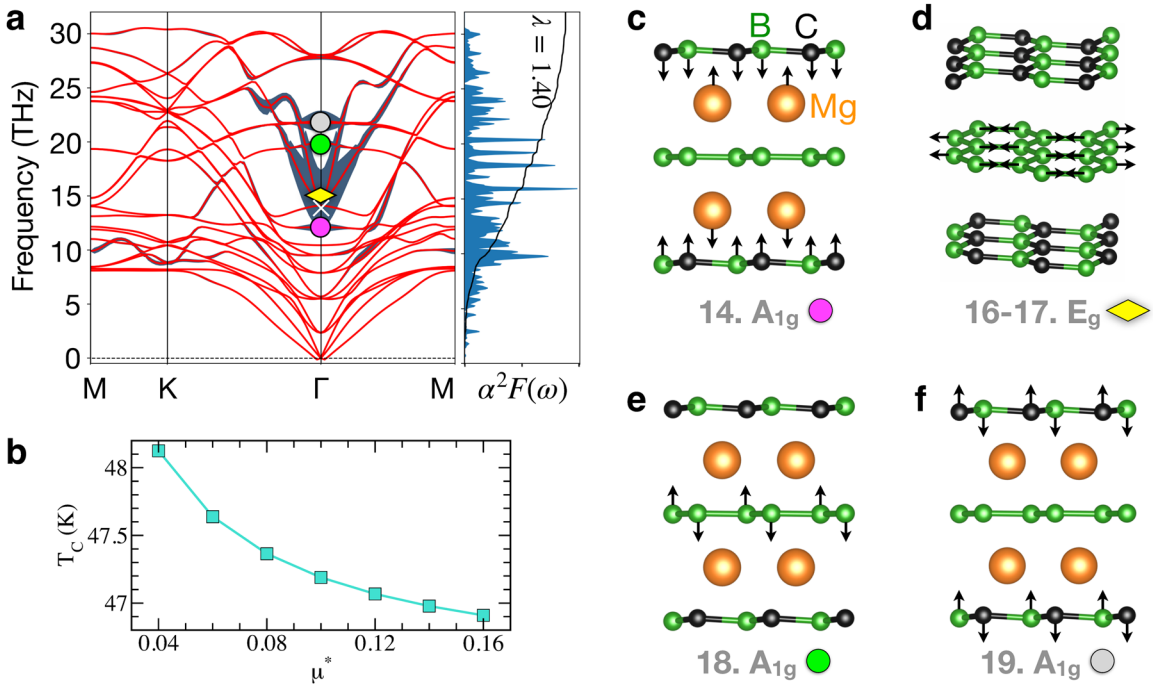

Fig. 3 Electron-phonon coupling. a Calculated phonon spectrum of $Mg_2B_4C_2$ monolayer with phonon linewidths $\lambda(\mathbf{q}, n)$ plotted using shaded blue color. To avoid large overlap of $\lambda(\mathbf{q}, n)$ with the phonon spectra, we have divided the intensity by a factor of two. The colored circles mark the three out-of-plane nondegenerate A_{1g} modes (indices 14, 18, and 19), and the yellow diamond marks one in-plane doubly degenerate E_g mode at Γ. These modes exhibit dominant el-ph coupling. The atomic displacement patterns corresponding to these modes are shown in (**c**–**f**). The nondegenerate A_{1u} mode (index 15) marked using symbol `×' does not contribute to the total el-ph coupling, although it appears to be buried in the large $\lambda(\mathbf{q}, n)$ of the E_g mode. The numerals 14, 15, 16, 17, 18, and 19 denote the phonon mode index as counted from the lowest to the highest frequency modes (i.e.,1-3 for acoustic modes). Mg atoms are omitted in (**c**) for the sake of clarity. The Eliashberg spectral function $\alpha^2F(\omega)$ along with the el-ph coupling constant λ in plotted in the right panel of (**a**). **b** Estimated T_c as a function of the μ^* parameter.

having the following mode symmetry at Γ:

$$\Gamma_{\text{acoustic}} = A_{2u} \oplus E_u, \text{ and}$$
$$\Gamma_{\text{optic}} = 4A_{1g} \oplus 3A_{2u} \oplus 3E_u \oplus 4E_g. \quad (1)$$

Here, A_{1g} and E_g are Raman-active modes, whereas, A_{2u} and E_u are infrared-active modes. In Fig. 3(c–f), we show the atomic vibration patterns for the four phonon modes, namely, three nondegenerate A_{1g} modes (indices 14, 18, and 19) and one degenerate E_g mode (indices 16-17), which exhibit the dominant el-ph coupling. All these A_{1g} modes correspond to the out-of-plane vibrations of the Mg, inner B-B, and outer B-C layers, while the E_g mode corresponds to the in-plane stretching of the inner B-B layer. The A_{1g} modes primarily modulate the el-ph coupling associated with the π bonded p_z orbitals contributing to the electron and hole pockets located at the BZ boundaries. Whereas, the doubly degenerate E_g mode couples with the σ bonded $p_{x,y}$ orbitals forming the hole pockets located at Γ. Here, it is worth noting that the higher frequency E_g modes (indices 21-22) that correspond to the in-plane stretching of the outer B-C layers do not make a significant contribution to the overall el-ph in this system, which is as expected since these modes modulate the occupied σ_{outer} bands located well-below the Fermi level at Γ [see Fig. 2(b)]. However, these modes may participate in superconductivity when the system is doped with p-type charge carriers[32].

Since the electronic and vibrational band structures of inner B-B and outer B-C layers are essentially independent of each other, we predicate that the reported properties of the studied $Mg_2B_4C_2$ monolayer would be retained even when the number of the inner B-B layers are repeated (until a critical thickness), thus making the system thicker. This feature might greatly simplify the eventual realization of superconductivity in $Mg_2B_4C_2$.

To quantify the superconducting properties of $Mg_2B_4C_2$ monolayer, we employ the McMillian-Allen-Dynes theory derived from the isotropic Migdal-Eliashberg formalism[75–77] which relies on the calculation of the el-ph coupling matrix elements within DFT. The calculated matrix elements correspond to the transition probabilities of different Kohn-Sham states induced by a change in the potential due to a small ionic displacement. Thus, these matrix elements provide the main ingredients to calculate the el-ph coupling strength and the Eliashberg spectral function $\alpha^2F(\omega)$ as a function of the phonon frequency ω. Since the physical process behind the phonon-mediated superconductivity is the exchange of a phonon between two electrons, a strong el-ph coupling is desired to achieve a high-T_c in a BCS superconductor. Theoretical details of such calculations are explained in numerous other papers[82,95,96].

In Fig. 3(a), we plot the calculated phonon linewidth $\lambda(\mathbf{q}, n)$ for each phonon mode n at each wave vector $\mathbf{q}$ using blue color. Note that the plotted phonon linewidth is scaled down by a factor of two to avoid large overlap with the neighboring phonon branches. The largest contribution to the total el-ph coupling strength comes from three nondegenerate A_{1g} modes and one doubly degenerate E_g mode, as marked in Fig. 3(a). We note that the A_{2u} mode (index 15), marked using `×' in Fig. 3(a), does not contribute to the total el-ph coupling, although it appears buried in the large $\lambda(\mathbf{q}, n)$ overlap from the E_g mode. Notably, in addition to the aforementioned A_{1g} and E_g phonon modes, various other modes make relatively smaller contributions to the overall el-ph coupling strength, as revealed by the Eliashberg spectral function $\alpha^2F(\omega)$ plot shown in the right panel of Fig. 3(a).

In addition to the el-ph coupling, the net phonon linewidth $\lambda(\mathbf{q}, n)$ can have some contribution from the phonon-phonon (ph-ph) interactions owing to the phonon anharmonicity[36]. Therefore, we thoroughly investigate ph-ph interactions by computing ph-ph linewidth using the ab-initio molecular dynamics simulations. In this approach, we mapped the forces, obtained from the

Table 2. Listing of superconducting parameters required for the prediction of T_c using the McMillian-Allen-Dynes formula for some reported 2D phonon-mediated superconductors (data for bulk MgB_2 are included for comparison). This table includes data of effective Coulomb screening parameter μ^*, electronic DOS at the Fermi level $N(E_F)$ (in states/spin/Ry/cell), logarithmic averaged phonon frequency ω_{log} (in K), total electron-phonon coupling constant λ, and estimated T_c (in K). Experimental T_c values are noted in the table (see the Supplementary Table 1 for more details).

Compounds	μ^*	$N(E_F)$	ω_{log}	λ	T_c	Ref.
B_2C	0.10		315	0.92	19	21
CaC_6	0.115		446	0.40	1.4	107
LiC_6	0.115		400	0.61	8.1	107
LiC_6				0.58 ± 0.05	5.9 [Exp.]	108
LiC_6	0.12/0.14/0.16			0.55	7.6/5.9/5.1	102
2H-$NbSe_2$				0.75	3.1 [Exp.]	7
2H-$NbSe_2$	0.15, 0.16		134, 145	0.84, 0.67	4.5, 2.7	110,111
C_6CaC_6					4.0 [Exp.]	112
C_6CaC_6	0.207/0.155				6.8/8.1	71,72,113
B_2O	0.10	5.4	250	0.75	10.3	17
LiBC	0.13	10.9		0.59	65	138
bulk MgB_2	0.05	9.8	707	0.73	40	38
bulk MgB_2	0.13	9.8		0.61	39	73
monolayer MgB_2	0.13	13.1		0.68	20	73
monolayer H-MgB_2	0.13	19.2		1.46	67	32
$Mg_2B_4C_2$	0.04	12.6	506	1.40	48.1	This work
	0.10				47.2	This work
	0.14				47.0	This work

finite-temperature molecular dynamics simulations, evaluated in a $3 \times 3 \times 1$ supercell onto a model Hamiltonian describing the lattice dynamics. This temperature dependent effective potential (TDEP) technique[97,98] enabled us to calculate the third-order response from the effective renormalized interatomic force constants. Our calculations revealed that the ph-ph linewidths are an order of magnitude smaller than the el-ph linewidths. The maximum value of obtained ph-ph linewidth is ~2 meV, which is much smaller compared to the el-ph linewidth values that are typically larger than ~ 70 meV in the studied system. This result implies that, although the system inherits some anharmonic effects, we can safely discard the ph-ph contributions in the study of its superconducting properties.

Based on the BCS theory of superconductivity and above results, we estimate the critical temperature T_c using the McMillian-Allen-Dynes formula[99–101]:

$$T_c = \frac{\omega_{log}}{1.2} exp\left[-\frac{1.04(1+\lambda)}{\lambda - \mu^*(1+0.62\lambda)}\right], \quad (2)$$

where ω_{log} is the logarithmic averaged phonon frequency, λ is the total el-ph coupling constant, and μ^* is the effective screened Coulomb repulsion constant with a typical value ranging from 0.04 to 0.16 (see Table 2)[21,35,36,38,56]. We obtain λ by integrating the cumulative frequency-dependent el-ph coupling $\lambda(\omega)$ given by the following expression:

$$\lambda(\omega) = 2\int_0^{\omega} \frac{\alpha^2 F(\omega)}{\omega} d\omega \quad (3)$$

We find a fairly large value of $\lambda = 1.40$, which is considerably larger than the one reported for bulk MgB_2 ($\lambda_{bulk} = 0.73$[38], and 0.61[36]). We observe that the estimated T_c does not vary drastically as a function of μ^*, as shown in Fig. 3(b). This is consistent with an earlier work by Choi et al.[36], which reported that the superconducting properties of MgB_2 are not very sensitive to the μ^* parameter within the isotropic McMillian-Allen-Dynes formalism. We note that for bulk MgB_2, $\mu^* = 0.05$ has been used to get the correct estimate of $T_c \sim 40$ K[38]. Therefore, using the McMillian-Allen-Dynes formula[99–101], we estimate the T_c of $Mg_2B_4C_2$ monolayer to be in the range 47–48 K without any doping or strain. Our results are consistent with a recent study[32] in which $T_c = 67\,K$ and $\lambda = 1.46$ was predicted in a hydrogenated MgB_2 monolayer by solving the fully anisotropic Eliasberg equations. We argue that the predicted T_c in $Mg_2B_4C_2$ monolayer can be further enhanced by biaxial strain[17,32] or by p-doping[32]. In passing, we would like to mention that the predicted T_c could moderately vary if a fully anisotropic Migdal-Eliashberg theory[32,36,82,102] or SC-DFT[103–106] is employed. This is particularly important here because the applicability of the McMillian-Allen-Dynes formula becomes limited in the case of large el-ph coupling.

In order to highlight the novelty of our results, in Table 2 we list the theoretical superconducting parameters along with the estimated T_c for some reported 2D phonon-mediated superconductors (see Supplementary Table 1). The good agreement between the experimental data for LiC_6[102,107,108], 2*H*-$NbSe_2$[7,109–111], and C_6CaC_6[112,113] and the corresponding theoretical results obtained from the McMillian-Allen-Dynes theory validate the the predictive power of the McMillian-Allen-Dynes theory.

SUMMARY

In summary, we present a 2D material $Mg_2B_4C_2$, similar to MgB_2, but with inert surfaces obtained by the replacement of outer B-B layers by B-C layers. Our calculations suggest that this structure is dynamically, elastically and mechanically stable. It also features a nontrivial topological electronic band structure together with a large el-ph coupling ($\lambda = 1.40$), which is more than twice as large as that of the bulk MgB_2 and comparable to that of in a hydrogenated monolayer MgB_2[32]. Use of the standard McMillian-Allen-Dynes theory predicts the superconducting transition temperature T_c to be in the range of 47–48 K without any doping or tuning of external parameters such as strain. To the best of our knowledge, this is among the highest predicted intrinsic T_c in a conventional BCS-type 2D superconductor. In addition to the large el-ph coupling, the presence of sharp and well-defined flat boundaries of the charge-carrier pockets at the Fermi surface imply the possible realization of Kohn-like divergencies and

charge-density-wave ordering in this 2D system, which calls for a dedicated study in future.

METHODS

DFT calculations

The electronic bands structure and phonon calculations were performed using density-functional theory (DFT) as implemented in the VASP[114–117]. The phonopy[118] and PyProcar[119] tools were used for the post-processing of data. The Perdew-Burke-Ernzerhof (PBE) exchange-correlation functional[120] and PAW pseudo-potentials[121,122] were used. The employed *k*-point grid for self-consistent calculations was $30 \times 30 \times 1$, and the cutoff for the kinetic energy of plane waves was set to 700 eV. A vacuum of thickness ~ 30 Å was added to avoid the periodic interactions along the *c*-axis. Since the spin-orbit coupling (SOC) effects were found to be negligible in the studied system, SOC was not included in the reported calculations. The elastic and mechanical properties were analyzed using the MechElastic code[123,124]. The exfoliation energy was calculated using four different exchange-correlation approximations: the (PBE) GGA approximation[120], the SCAN[125] meta-GGA, vdW-DF2 GGA functional[126], and SCAN together with the rVV10 correlation functional (SCAN+rVV10)[127]. The topological properties of $Mg_2B_4C_2$ were studied by fitting the DFT calculated bandstructure to a real space tight-binding Hamiltonian obtained using the maximally localized Wannier functions (MLWFs) approach[128,129]. The local density of states at (100) and (010) edges were calculated for 60 unit cells thick nano-ribbons using the WannierTools package[129] with vacuum added along the *c*-axis of the ribbon.

For the electron-phonon coupling matrix elements calculations, we used the abinit package[130–134]. We employed norm conserving pseudopotentials (using the ONCVPSP scheme of Hamann[135]), and a plane wave basis set up to kinetic energies of 35 Ha. Cell parameters were optimized by using the PBE exchange-correlation functional as in VASP calculations. We used a uniform grid of $18 \times 18 \times 1$ for the ground state calculations, and a phonon grid of $9 \times 9 \times 1$ for the phonon part. A total of 288 el-ph matrix elements were calculated. Calculations of the phonon interatomic force constants, and the el-ph coupling matrix elements performed in this work used the second-order perturbation theory[136,137]. The temperature dependent effective potential (TDEP) technique[97,98] was used to study the phonon-phonon interactions and phonon anharmonic effects.

DATA AVAILABILITY

The data that support the findings of this study are available from the corresponding authors upon reasonable request.

CODE AVAILABILITY

The first-principles DFT calculations were performed using the privately-licensed VASP code, and the ABINIT code, which is available at https://www.abinit.org under the GNU General Public License.

Received: 4 May 2021; Accepted: 2 March 2022;
Published online: 01 April 2022

REFERENCES

1. Uchihashi, T. Two-dimensional superconductors with atomic-scale thickness. *Supercond. Sci. Technol.* **30**, 013002 (2017).
2. Saito, Y., Nojima, T. & Iwasa, Y. Highly crystalline 2D superconductors. *Nat. Rev. Mater.* **2**, 16094 (2017).
3. Jiang, D. et al. High-Tc superconductivity in ultrathin $Bi_2Sr_2CaCu_2O_{8+x}$ down to half-unit-cell thickness by protection with graphene. *Nat Commun.* **5**, 5708 (2014).
4. Kamihara, Y., Watanabe, T., Hirano, M. & Hosono, H. Iron-based layered superconductor $La[O_{1-x}F_x]FeAs$ (x = 0.05–0.12) with Tc = 26 K. *J. American Chemical Soc.* **130**, 3296–3297 (2008).
5. Brun, C., Cren, T. & RodiTchev, D. Review of 2D superconductivity: The ultimate case of epitaxial monolayers. *Superconductor Sci. Technol.* **30**, 013003 (2016).
6. Frindt, R. F. Superconductivity in ultrathin $NbSe_2$ layers. *Phys. Rev. Lett.* **28**, 299–301 (1972).
7. Xi, X. et al. Strongly enhanced charge-density-wave order in monolayer NbSe2. *Nature Nanotechnol.* **10**, 765–769 (2015).
8. Ugeda, M. M. et al. Characterization of collective ground states in single-layer $NbSe_2$. *Nat. Phys.* **12**, 92–97 (2016).
9. Li, Y.-L. et al. Superconductivity in the van der Waals layered compound PS_2. *Phys. Rev. B* **99**, 220503 (2019).
10. Novoselov, K. S., Mishchenko, A., Carvalho, A. & Castro Neto, A. H. 2D materials and van der Waals heterostructures. *Science* **353**, https://science.sciencemag.org/content/353/6298/aac9439 (2016).
11. Yabuki, N. et al. Supercurrent in van der Waals Josephson junction. *Nat. Commun.* **7**, 10616 (2016).
12. Xi, X. et al. Ising pairing in superconducting $NbSe_2$ atomic layers. *Nature Phys.* **12**, 139–143 (2016).
13. Xu, B. Z. & Beckman, S. P. Quantum confinement induced band gaps in MgB_2 nanosheets. *2D Mater.* **3**, 031003 (2016).
14. de la Barrera, S. C. et al. Tuning Ising superconductivity with layer and spin–orbit coupling in two-dimensional transition-metal dichalcogenides. *Nat. Commun.* **9**, 1427 (2018).
15. Bao, L. et al. Thickness dependence of superconductivity in single-crystal $Ta_4Pd_3Te_{16}$ nanoribbons. *Appl. Phys. Lett.* **113**, 022603 (2018).
16. Yan, R. et al. Thickness dependence of superconductivity in ultrathin NbS_2. *Appl. Phys. Express* **12**, 023008 (2019).
17. Yan, L. et al. Theoretical dissection of superconductivity in two-dimensional honeycomb borophene oxide B_2O crystal with a high stability. *npj Computational Mater.* **6**, 94 (2020).
18. Penev, E. S., Kutana, A. & Yakobson, B. I. Can two-dimensional boron superconduct? *Nano Lett.* **16**, 2522–2526 (2016).
19. Wang, B.-T. et al. Superconductivity in two-dimensional phosphorus carbide (β_0-PC). *Phys. Chem. Chem. Phys.* **20**, 12362–12367 (2018).
20. Lei, J., Kutana, A. & Yakobson, B. I. Predicting stable phase monolayer Mo_2C (MXene), a superconductor with chemically-tunable critical temperature. *J. Mater. Chem. C* **5**, 3438–3444 (2017).
21. Dai, J., Li, Z., Yang, J. & Hou, J. A first-principles prediction of two-dimensional superconductivity in pristine B_2C single layers. *Nanoscale* **4**, 3032–3035 (2012).
22. Gao, M., Li, Q.-Z., Yan, X.-W. & Wang, J. Prediction of phonon-mediated superconductivity in borophene. *Phys. Rev. B* **95**, 024505 (2017).
23. Qu, Z. et al. Prediction of strain-induced phonon-mediated superconductivity in monolayer YS. *J. Mater. Chem. C* **7**, 11184–11190 (2019).
24. Yan, L. et al. Novel structures of two-dimensional tungsten boride and their superconductivity. *Phys. Chem. Chem. Phys.* **21**, 15327–15338 (2019).
25. Rosner, H., Kitaigorodsky, A. & Pickett, W. E. Prediction of high T_c superconductivity in hole-doped LiBC. *Phys. Rev. Lett.* **88**, 127001 (2002).
26. Pogrebnyakov, A. V. et al. Enhancement of the superconducting transition temperature of MgB_2 by a strain-induced bond-stretching mode softening. *Phys. Rev. Lett.* **93**, 147006 (2004).
27. Weller, T. E., Ellerby, M., Saxena, S. S., Smith, R. P. & Skipper, N. T. Superconductivity in the intercalated graphite compounds C_6Yb and C_6Ca. *Nat. Phys.* **1**, 39–41 (2005).
28. Gauzzi, A. et al. Enhancement of superconductivity and evidence of structural instability in intercalated graphite CaC_6 under high pressure. *Phys. Rev. Lett.* **98**, 067002 (2007).
29. Savini, G., Ferrari, A. C. & Giustino, F. First-principles prediction of doped graphane as a high-temperature electron-phonon superconductor. *Phys. Rev. Lett.* **105**, 037002 (2010).
30. Wu, Q. et al. Versatile titanium silicide monolayers with prominent ferromagnetic, catalytic, and superconducting properties: Theoretical prediction. *J. Phys. Chem. Lett.* **7**, 3723–3729 (2016).
31. Zhang, J.-J. & Dong, S. Superconductivity of monolayer Mo_2C: The key role of functional groups. *J. Chem. Phys.* **146**, 034705 (2017).
32. Bekaert, J., Petrov, M., Aperis, A., Oppeneer, P. M. & Milošević, M. V. Hydrogen-induced high-temperature superconductivity in two-dimensional materials: The example of hydrogenated monolayer mgb_2. *Phys. Rev. Lett.* **123**, 077001 (2019).
33. Kruchinin, S. P. Physics of high-Tc superconductors. *Rev. Theoretical Sci.* **2**, 124–145 (2014).
34. Nagamatsu, J., Nakagawa, N., Muranaka, T., Zenitani, Y. & Akimitsu, J. Superconductivity at 39 K in magnesium diboride. *Nature* **410**, 63–64 (2001).
35. Choi, H. J., Roundy, D., Sun, H., Cohen, M. L. & Louie, S. G. The origin of the anomalous superconducting properties of MgB_2. *Nature* **418**, 758–760 (2002).
36. Choi, H. J., Roundy, D., Sun, H., Cohen, M. L. & Louie, S. G. First-principles calculation of the superconducting transition in MgB_2 within the anisotropic Eliashberg formalism. *Phys. Rev. B* **66**, 020513 (2002).
37. An, J. M. & Pickett, W. E. Superconductivity of MgB_2: Covalent bonds driven metallic. *Phys. Rev. Lett.* **86**, 4366–4369 (2001).
38. Bohnen, K.-P., Heid, R. & Renker, B. Phonon dispersion and electron-phonon coupling in MgB_2 and AlB_2. *Phys. Rev. Lett.* **86**, 5771–5774 (2001).
39. Iavarone, M. et al. Two-band superconductivity in MgB_2. *Phys. Rev. Lett.* **89**, 187002 (2002).

40. Pickett, W. Mind the double gap. *Nature* **418**, 733–734 (2002).
41. Mazin, I. & Antropov, V. Electronic structure, electron-phonon coupling, and multiband effects in MgB_2. *Physica C Supercond.* **385**, 49–65 (2003).
42. Xi, X. X. Two-band superconductor magnesium diboride. *Rep. Prog. Phys.* **71**, 116501 (2008).
43. Pickett, W. The next breakthrough in phonon-mediated superconductivity. *Physica C: Superconductivity* **468**, 126–135 (2008).
44. Pickett, W. E. Design for a room-temperature superconductor. *J Superconductivity Novel Magnetism* **19**, 291–297 (2006).
45. Yildirim, T. et al. Giant anharmonicity and nonlinear electron-phonon coupling in MgB_2: A combined first-principles calculation and neutron scattering study. *Phys. Rev. Lett.* **87**, 037001 (2001).
46. Szabó, P. et al. Evidence for two superconducting energy gaps in MgB_2 by point-contact spectroscopy. *Phys. Rev. Lett.* **87**, 137005 (2001).
47. Rosner, H., An, J. M., Pickett, W. E. & Drechsler, S.-L. Fermi surfaces of diborides: MgB_2 and ZrB_2. *Phys. Rev. B* **66**, 024521 (2002).
48. Choi, H. J., Cohen, M. L. & Louie, S. G. Anisotropic Eliashberg theory of MgB_2: T_c, isotope effects, superconducting energy gaps, quasiparticles, and specific heat. *Physica C Supercond.* **385**, 66–74 (2003).
49. Kortus, J. Current progress in the theoretical understanding of MgB_2. *Physica C Supercond.* **456**, 54–62 (2007).
50. Pickett, W., Klein, B. & Papaconstantopoulos, D. Theoretical prediction of MoN as a high Tc superconductor. *Physica B+C* **107**, 667–668 (1981).
51. Pickett, W., An, J., Rosner, H. & Savrasov, S. Role of two dimensionality in MgB_2. *Physica C: Superconductivity* **387**, 117–121 (2003).
52. Boeri, L. et al. The 2021 room-temperature superconductivity roadmap. *J Phys: Condensed Matter*. https://doi.org/10.1088/1361-648X/ac2864 (2021).
53. Verma, A. K. et al. Possible high-temperature superconductivity in hole-doped MgB_2C_2. *EPL* **63**, 743 (2003).
54. Rosner, H., Kitaigorodsky, A. & Pickett, W. Prediction of high Tc superconductivity in hole-doped LiBC. *Phys. Rev. Lett.* **88**, 1270011–1270014 (2002).
55. An, J. M., Savrasov, S. Y., Rosner, H. & Pickett, W. E. Extreme electron-phonon coupling in boron-based layered superconductors. *Phys. Rev. B* **66**, 220502 (2002).
56. Choi, H. J., Louie, S. G. & Cohen, M. L. Prediction of superconducting properties of CaB_2 using anisotropic Eliashberg theory. *Phys. Rev. B* **80**, 064503 (2009).
57. Miao, R., Huang, G. & Yang, J. First-principles prediction of MgB_2-like NaBC: A more promising high-temperature superconducting material than LiBC. *Solid State Commun.* **233**, 30–34 (2016).
58. Bersier, C. et al. Electronic, vibrational, and superconducting properties of CaBeSi: First-principles calculations. *Phys. Rev. B* **79**, 104503 (2009).
59. Norman, M. R. Materials design for new superconductors. *Rep. Prog. Phys.* **79**, 074502 (2016).
60. Stanev, V. et al. Machine learning modeling of superconducting critical temperature. *npj Computational Mater.* **4**, 29 (2018).
61. Zhai, H., Munoz, F. & Alexandrova, A. N. Strain to alter the covalency and superconductivity in transition metal diborides. *J. Mater. Chem. C* **7**, 10700–10707 (2019).
62. Klintenberg, M. & Eriksson, O. Possible high-temperature superconductors predicted from electronic structure and data-filtering algorithms. *Comput. Mater. Sci.* **67**, 282–286 (2013).
63. Kolmogorov, A. N. et al. New superconducting and semiconducting fe-b compounds predicted with an ab initio evolutionary search. *Phys. Rev. Lett.* **105**, 217003 (2010).
64. Gou, H. et al. Discovery of a superhard iron tetraboride superconductor. *Phys. Rev. Lett.* **111**, 157002 (2013).
65. Liu, H., Naumov, I. I., Hoffmann, R., Ashcroft, N. W. & Hemley, R. J. Potential high-tc superconducting lanthanum and yttrium hydrides at high pressure. *Proc. Nat. Acad. Sci.* **114**, 6990–6995 (2017).
66. Peng, F. et al. Hydrogen clathrate structures in rare earth hydrides at high pressures: Possible route to room-temperature superconductivity. *Phys. Rev. Lett.* **119**, 107001 (2017).
67. Liu, H. et al. Dynamics and superconductivity in compressed lanthanum superhydride. *Phys. Rev. B* **98**, 100102 (2018).
68. Drozdov, A. P. et al. Superconductivity at 250 k in lanthanum hydride under high pressures. *Nature* **569**, 528–531 (2019).
69. Naito, M. & Ueda, K. MgB_2 thin films for superconducting electronics. *Supercond. Sci. Technol.* **17**, R1–R18 (2004).
70. Xi, X. X. MgB_2 thin films. *Supercond. Sci. Technol.* **22**, 043001 (2009).
71. Mazin, I. & Balatsky, A. Superconductivity in ca-intercalated bilayer graphene. *Philosophical Magazine Lett.* **90**, 731–738 (2010).
72. Jishi, R., Guzman, D. & Alyahyaei, H. Theoretical investigation of two-dimensional superconductivity in intercalated graphene layers. *Adv. Studies Theor. Phys.* **5**, 703–716 (2011).
73. Bekaert, J., Aperis, A., Partoens, B., Oppeneer, P. M. & Milošević, M. V. Evolution of multigap superconductivity in the atomically thin limit: Strain-enhanced three-gap superconductivity in monolayer MgB_2. *Phys. Rev. B* **96**, 094510 (2017).
74. Bekaert, J. et al. Free surfaces recast superconductivity in few-monolayer MgB_2: Combined first-principles and ARPES demonstration. *Sci. Rep.* **7**, 14458 (2017).
75. Migdal, A. Interaction between electrons and lattice vibrations in a normal metal. *Sov. Phys. JETP* **7**, 996–1001 (1958).
76. Eliashberg, G. Interactions between electrons and lattice vibrations in a superconductor. *Sov. Phys. JETP* **11**, 696–702 (1960).
77. Allen, P. B. & Mitrović, B. Theory of superconducting Tc. vol. 37 of *Solid State Physics*, 1 – 92 (Academic Press, 1983). http://www.sciencedirect.com/science/article/pii/S0081194708606657.
78. Geim, A. K. & Grigorieva, I. V. Van der Waals heterostructures. *Nature* **499**, 419–425 (2013).
79. Li, J., Martin, I., Büttiker, M. & Morpurgo, A. F. Marginal topological properties of graphene: a comparison with topological insulators. *Phys. Scr.* **2012**, 014021 (2012).
80. Mounet, N. et al. Two-dimensional materials from high-throughput computational exfoliation of experimentally known compounds. *Nat. Nanotechnol.* **13**, 246–252 (2018).
81. Iavarone, M. et al. MgB_2: Directional tunnelling and two-band superconductivity. *Superconductor Sci. Technol.* **16**, 156–161 (2002).
82. Margine, E. R. & Giustino, F. Anisotropic Migdal-Eliashberg theory using Wannier functions. *Phys. Rev. B* **87**, 024505 (2013).
83. Mou, D. et al. Momentum dependence of the superconducting gap and in-gap states in MgB_2 multiband superconductor. *Phys. Rev. B* **91**, 214519 (2015).
84. Aperis, A., Maldonado, P. & Oppeneer, P. M. Ab initio theory of magnetic-field-induced odd-frequency two-band superconductivity in MgB_2. *Phys. Rev. B* **92**, 054516 (2015).
85. Kortus, J., Mazin, I. I., Belashchenko, K. D., Antropov, V. P. & Boyer, L. L. Superconductivity of metallic boron in MgB_2. *Phys. Rev. Lett.* **86**, 4656–4659 (2001).
86. Ye, J. T. et al. Superconducting dome in a gate-tuned band insulator. *Science* **338**, 1193–1196 (2012).
87. Jin, K.-H. et al. Topological superconducting phase in high-Tc superconductor MgB_2 with Dirac–nodal-line Fermions. *npj Computational Mat.* **5**, 57 (2019).
88. Kohn, W. Image of the Fermi surface in the vibration spectrum of a metal. *Phys. Rev. Lett.* **2**, 393–394 (1959).
89. Grüner, G. The dynamics of charge-density waves. *Rev. Mod. Phys.* **60**, 1129–1181 (1988).
90. Zhu, X., Cao, Y., Zhang, J., Plummer, E. W. & Guo, J. Classification of charge density waves based on their nature. *Proc. Nat. Acad. Sci.* **112**, 2367–2371 (2015).
91. Gibson, Q. D. et al. Three-dimensional Dirac semimetals: Design principles and predictions of new materials. *Phys. Rev. B* **91**, 205128 (2015).
92. Kobayashi, S. & Sato, M. Topological superconductivity in Dirac semimetals. *Phys. Rev. Lett.* **115**, 187001 (2015).
93. Fu, L. & Kane, C. L. Topological insulators with inversion symmetry. *Phys. Rev. B* **76**, 045302 (2007).
94. Zhou, X. et al. Observation of topological surface states in the high-temperature superconductor MgB_2. *Phys. Rev. B* **100**, 184511 (2019).
95. Giustino, F. Electron-phonon interactions from first principles. *Rev. Mod. Phys.* **89**, 015003 (2017).
96. Giustino, F., Cohen, M. L. & Louie, S. G. Electron-phonon interaction using Wannier functions. *Phys. Rev. B* **76**, 165108 (2007).
97. Hellman, O. & Abrikosov, I. A. Temperature-dependent effective third-order interatomic force constants from first principles. *Phys. Rev. B* **88**, 144301 (2013).
98. Hellman, O., Steneteg, P., Abrikosov, I. A. & Simak, S. I. Temperature dependent effective potential method for accurate free energy calculations of solids. *Phys. Rev. B* **87**, 104111 (2013).
99. Bardeen, J., Cooper, L. N. & Schrieffer, J. R. Theory of superconductivity. *Phys. Rev.* **108**, 1175–1204 (1957).
100. McMillan, W. L. Transition temperature of strong-coupled superconductors. *Phys. Rev.* **167**, 331–344 (1968).
101. Allen, P. B. & Dynes, R. C. Transition temperature of strong-coupled superconductors reanalyzed. *Phys. Rev. B* **12**, 905–922 (1975).
102. Zheng, J.-J. & Margine, E. R. First-principles calculations of the superconducting properties in Li-decorated monolayer graphene within the anisotropic Migdal-Eliashberg formalism. *Phys. Rev. B* **94**, 064509 (2016).
103. Lüders, M. et al. Ab initio theory of superconductivity. i. density functional formalism and approximate functionals. *Phys. Rev. B* **72**, 024545 (2005).
104. Marques, M. A. L. et al. Ab initio theory of superconductivity. ii. application to elemental metals. *Phys. Rev. B* **72**, 024546 (2005).
105. Sanna, A. et al. Anisotropic gap of superconducting cac_6: A first-principles density functional calculation. *Phys. Rev. B* **75**, 020511 (2007).
106. Sanna, A., Pellegrini, C. & Gross, E. K. U. Combining eliashberg theory with density functional theory for the accurate prediction of superconducting transition temperatures and gap functions. *Phys. Rev. Lett.* **125**, 057001 (2020).

107. Profeta, G., Calandra, M. & Mauri, F. Phonon-mediated superconductivity in graphene by lithium deposition. *Nat. Phys.* **8**, 131–134 (2012).
108. Ludbrook, B. M. et al. Evidence for superconductivity in Li-decorated monolayer graphene. *Proc. Natl. Acad. Sci.* **112**, 11795–11799 (2015).
109. Heil, C. et al. Origin of superconductivity and latent charge density wave in NbS_2. *Phys. Rev. Lett.* **119**, 087003 (2017).
110. Lian, C.-S., Si, C. & Duan, W. Unveiling charge-density wave, superconductivity, and their competitive nature in two-dimensional $NbSe_2$. *Nano Lett.* **18**, 2924–2929 (2018).
111. Zheng, F. & Feng, J. Electron-phonon coupling and the coexistence of superconductivity and charge-density wave in monolayer $NbSe_2$. *Phys. Rev. B* **99**, 161119 (2019).
112. Ichinokura, S., Sugawara, K., Takayama, A., Takahashi, T. & Hasegawa, S. Superconducting calcium-intercalated bilayer graphene. *ACS Nano* **10**, 2761–2765 (2016).
113. Margine, E. R., Lambert, H. & Giustino, F. Electron-phonon interaction and pairing mechanism in superconducting Ca-intercalated bilayer graphene. *Scientific Rep.* **6**, 21414 (2016).
114. Kresse, G. & Hafner, J. Ab initio molecular dynamics for liquid metals. *Phys. Rev. B* **47**, 558–561 (1993).
115. Kresse, G. & Hafner, J. Ab initio molecular-dynamics simulation of the liquid-metal amorphous-semiconductor transition in germanium. *Phys. Rev. B* **49**, 14251–14269 (1994).
116. Kresse, G. & Furthmüller, J. Efficiency of ab-initio total energy calculations for metals and semiconductors using a plane-wave basis set. *Comput. Mat. Sci.* **6**, 15 (1996).
117. Kresse, G. & Furthmüller, J. Efficient iterative schemes for ab initio total-energy calculations using a plane-wave basis set. *Phys. Rev. B* **54**, 11169–11186 (1996).
118. Togo, A. & Tanaka, I. First principles phonon calculations in materials science. *Scr. Mater.* **108**, 1–5 (2015).
119. Herath, U. et al. PyProcar: A Python library for electronic structure pre/post-processing. *Comp. Phys. Commun.* **251**, 107080 (2020).
120. Perdew, J. P., Burke, K. & Ernzerhof, M. Generalized gradient approximation made simple. *Phys. Rev. Lett.* **77**, 3865–3868 (1996).
121. Blöchl, P. E. Projector augmented-wave method. *Phys. Rev. B* **50**, 17953–17979 (1994).
122. Kresse, G. & Joubert, D. From ultrasoft pseudopotentials to the projector augmented-wave method. *Phys. Rev. B* **59**, 1758–1775 (1999).
123. Singh, S., Valencia-Jaime, I., Pavlic, O. & Romero, A. H. Elastic, mechanical, and thermodynamic properties of Bi-Sb binaries: Effect of spin-orbit coupling. *Phys. Rev. B* **97**, 054108 (2018).
124. Singh, S. et al. Mechelastic: A python library for analysis of mechanical and elastic properties of bulk and 2d materials. *Comp. Phys. Commun.* **267**, 108068 (2021).
125. Sun, J., Ruzsinszky, A. & Perdew, J. P. Strongly constrained and appropriately normed semilocal density functional. *Phys. Rev. Lett.* **115**, 036402 (2015).
126. Lee, K., Murray, E. D., Kong, L., Lundqvist, B. I. & Langreth, D. C. Higher-accuracy van der waals density functional. *Phys. Rev. B* **82**, 081101 (2010).
127. Peng, H., Yang, Z.-H., Perdew, J. P. & Sun, J. Versatile van der waals density functional based on a meta-generalized gradient approximation. *Phys. Rev. X* **6**, 041005 (2016).
128. Mostofi, A. A. et al. An updated version of wannier90: A tool for obtaining maximally-localised Wannier functions. *Comput. Phys. Commun.* **185**, 2309–2310 (2014).
129. Wu, Q., Zhang, S., Song, H.-F., Troyer, M. & Soluyanov, A. A. WannierTools: An open-source software package for novel topological materials. *Comput. Phys. Commun.* **224**, 405–416 (2018).
130. Gonze, X. et al. First-principles computation of material properties: The abinit software project. *Comput. Mater. Sci.* **25**, 478–492 (2002).
131. Gonze, X. A brief introduction to the abinit software package. *Z. Kristallogr. Cryst. Mater.* **220**, 558–562 (2005).
132. Gonze, X. et al. Abinit: First-principles approach to material and nanosystem properties. *Comp. Phys. Commun.* **180**, 2582–2615 (2009).
133. Gonze, X. et al. Recent developments in the abinit software package. *Comput. Phys. Commun.* **205**, 106–131 (2016).
134. Romero, A. H. et al. Abinit: Overview and focus on selected capabilities. *J. Chem. Phys.* **152**, 124102 (2020).
135. Hamann, D. Optimized norm-conserving vanderbilt pseudopotentials. *Phys. Rev. B* **88**, 085117 (2013).
136. Baroni, S., De Gironcoli, S., Dal Corso, A. & Giannozzi, P. Phonons and related crystal properties from density-functional perturbation theory. *Rev. Mod. Phys.* **73**, 515 (2001).
137. Gonze, X. Adiabatic density-functional perturbation theory. *Phys. Rev. A* **52**, 1096 (1995).
138. Modak, P., Verma, A. K. & Mishra, A. K. Prediction of superconductivity at 70 k in a pristine monolayer of libc. *Phys. Rev. B* **104**, 054504 (2021).

ACKNOWLEDGEMENTS

This work was supported in part by Fondecyt Grants No. 1191353 (F.M.), 3200697 (J.D.M.), 1180175 (V.E.), 1190361(E.M.), Center for the Development of Nanoscience and Nanotechnology CEDENNA AFB180001, and from Conicyt PIA/Anillo ACT192023. S.S., K.R., and D.V. acknowledge the support from Office of Naval Research (ONR) Grants N00014-21-1-2107, N00014-19-1-2073, and N00014-16-1-2951. D.V. acknowledges support from National Science Foundation (NSF) grant DMR-1954856. We also thank the NSF CAREER Award CHE-1351968 to A.N.A. This research was partially supported by the supercomputing infrastructure of the NLHPC (ECM-02) and XSEDE which is supported by National Science Foundation grant number ACI-1053575. The authors also acknowledge the support from the Texas Advances Computer Center (with the Stampede2 and Bridges supercomputers). This work was supported by the U.S. Department of Energy (DOE), Office of Science, Basic Energy Sciences under awards DE-SC0020353 (S.S.) and DE-SC0021375 (A.H.R.).

AUTHOR CONTRIBUTIONS

S.S., D.V., K.R., and F.M. carried out the analysis of structural stability, electronic structure, and phonon spectra. A.H.R. performed the calculations of electron-phonon and phonon-phonon coupling, and estimated the superconducting transition temperature. J.D.M., V.E, and E.M. analyzed the electronic bandstructure of thicker slabs and calculated the exfoliation energies. A.N.A. and F.M. conceived the idea of surface passivation. S.S. and F.M. wrote the manuscript. All authors discussed the results and reviewed the manuscript.

COMPETING INTERESTS

The authors declare no competing interests.

ADDITIONAL INFORMATION

Supplementary information The online version contains supplementary material available at https://doi.org/10.1038/s41535-022-00446-6.

Correspondence and requests for materials should be addressed to Sobhit Singh, Aldo H. Romero or Francisco Muñoz.